Intershell-correlation-induced time delay in atomic photoionization

D. A. Keating, S. T. Manson, V. K. Dolmatov, A. Mandal, P. C. Deshmukh, Faiza Naseem, and A. S. Kheifets

Phys. Rev. A **98**, 013420 — Published 24 July 2018

DOI: 10.1103/PhysRevA.98.013420

Inter-shell correlation-induced time delay in atomic photoionization

D. A. Keating, S. T. Manson
Department of Physics and Astronomy, Georgia State University, Atlanta, 30303, U.S.A.

V. K. Dolmatov
Department of Physics and Earth Science, University of North Alabama, Florence, AL 35632, USA

A. Mandal
Department of Physics, Indian Institute of Science Education and Research Tirupati, Tirupati 517507, India

P. C. Deshmukh
Department of Physics, Indian Institute of Technology Tirupati, Tirupati, 517506, India
Department of Physics, Indian Institute of Science Education and Research Tirupati, Tirupati 517507, India

Faiza Naseem, A. S. Kheifets
Research School of Physics and Engineering, The Australian National University, Canberra ACT 0200, Australia[*]

(Dated: July 6, 2018)

We predict an observable Wigner time delay in outer atomic shell photoionization near inner shell thresholds. The near-threshold increase of time delay is caused by inter-shell correlation and serves as a sensitive probe of this effect. The time delay increase is present even when the inner and outer shell thresholds are hundreds of electron volts apart. We illustrate this observation by several prototypical examples in noble gas atoms from Ne to Kr. In our study, We employ the random phase approximation with exchange (RPAE) and its relativistic generalization RRPA. We also support our findings by a simplified, yet quite insightful, treatment within the lowest order perturbation theory.

PACS numbers: 32.80.Aa 32.80.Fb 32.80.RM 32.80.Zb 42.50.Hz

I. INTRODUCTION

The effect of inter-shell correlation is an established phenomenon in atomic photoionization. This effect manifests itself particularly clearly in valence subshells of noble gas atoms which leads to a significant modification of the photoionization cross section and angular anisotropy parameters. This modification can be accounted for accurately within the random phase approximation with exchange (RPAE) [1] and its relativistic analogue, the relativistic random-phase approximationn (RRPA) [2, 3]. Correlation of the outer atomic shell with its inner counterparts is known to be weaker as the corresponding thresholds can be separated by hundreds of electron volts [4]. The discrete spectrum below the inner shell threshold manifests itself by series of auto-ionization resonances in the outer shell photoionization cross section [5]. However, the outer shell photoionization cross section can remain relatively flat and unaffected immediately above the inner shell threshold. This is so because the inter-electron Coulomb interaction that drives the inter-shell correlation is weak in atomic shells that are so far apart.

At the same time, the opening of the inner shell at a sufficiently large photon energy can add a sizable phase shift to the photoionization amplitude of the outer shell even though the modulus of the amplitude is only changed slightly. A rapid change of the phase occurs in an interval of several electron volts and the energy derivative of the phase is large. When this derivative is converted to the time delay by the Wigner formula [6]

$$\tau_W = \frac{\partial \arg f(\epsilon)}{\partial \epsilon} = \mathrm{Im} \frac{f'(\epsilon)}{f(\epsilon)} \tag{1}$$

it is translated into a measurable quantity of the order of 10 as (1 as = 10^{-18} s). This time delay becomes a sensitive probe of inter-shell correlation in a situation where measurement of the total photoionization cross section of the outer shell brings little evidence of this correlation. We note that modern experiments can detect photoemission time delay with a sub-attosecond precision [7] and attosecond streaking measurements can now be expanded to the soft-x-ray range up to 350 eV [8].

We illustrate this effect by considering several prototypical examples in inner and outer shells of noble gas atoms. We employ the RPAE methodology as described in [9] and its relativistic counterpart RRPA [2, 3]. We intentionally leave out the question of the probe field and associated effect of the laser-Coulomb coupling which modifies the atomic time delay as

$$\tau_a = \tau_W + \tau_{\mathrm{CLC}} \tag{2}$$

---

[*] Electronic address: `A.Kheifets@anu.edu.au`

The CLC, known also as continuum-continuum (CC) correction, is commonly represented by a hydrogenic approximation [10, 11]. Irrespective of the accuracy of this representation, at such large photoelectron energies, this correction should be vanishingly small. So in the following we concentrate solely on the Wigner component of the time-delay τ_W. Atomic units are used throughout the paper unless otherwise is specified. One atomic unit of time is equal to 24.2 as and 1 atomic unit of energy is equal to 2 Ry or 27.2 eV .

II. THEORY

A. Random phase approximation

The random phase approximation was applied to to calculate photoionization cross sections and angular anisotropy parameters in valence shell of noble gas atoms some forty years ago [12]. Since then, it became a standard technique to account for inter-shell correlation in valence shell photoionization in these atoms (see [1] and references therein). It had been generalized for inner shell photoionization by adopting experimental ionization thresholds and including the lifetime of the inner vacancy due to its Auger decay. These generalizations are collectively termed GRPAE [13]. The RPAE [14] and RRPA [15] had been previously employed to evaluate the Wigner time delay in valence and inner shells of noble gas atoms. Therefore we describe the theory of these methods only briefly.

We adopt the notation of [14] and write the (nonrelativistic) amplitude of photoionization from a bound state i to an ingoing scattering state defined by the photoelectron momentum $\boldsymbol{k}$ as

$$f_{n_i\ell_i}(\boldsymbol{k}) \equiv \langle \psi^{(-)}_{\boldsymbol{k}} | \hat{z} | \phi_i \rangle \ \propto \sum_{\substack{l=l_i\pm1\\ m=m_i}} e^{i\delta_\ell(E)} i^{-l} Y_{\ell m}(\hat{\boldsymbol{k}}) \quad (3)$$
$$\times \begin{pmatrix} \ell & 1 & \ell_i \\ -m & 0 & m_i \end{pmatrix} d_{ik} \quad , \quad d_{ik} \equiv \langle k\ell \| \, r \, \| n_i\ell_i \rangle$$

These bound and continuous states are orthogonal and are eigenstates of the frozen core atomic Hamiltonian. We consider the case of linearly polarized incident photons whose polarization direction is taken as the quantization $\hat{z}$ axis. The proportionality constant depends on the normalization of the final-state scattering wave function. The reduced dipole matrix element, stripped of all the angular momentum projections, is defined as

$$\langle k\ell \| \, r \, \| n_i\ell_i \rangle = \hat{\ell}\hat{\ell}_i \begin{pmatrix} \ell & 1 & \ell_i \\ 0 & 0 & 0 \end{pmatrix} \int r^2 dr \, R_{k\ell}(r) \, r \, R_{n_i\ell_i}(r) \ , \quad (4)$$

where we use a shortcut, $\hat{\ell} = \sqrt{2\ell+1}$. Eqs. (3) and (4) employ the length gauge of the electromagnetic interaction. The analogous expressions in the velocity gauge contain the ∇_z and $\partial/\partial r$ operators, respectively. The gauge invariance of the present results serves as an addition test on the accuracy of the present calculations. We note that for two competing ionization channels $l = l_i \pm 1$, the phase of the amplitude (3) depends on the direction of the photoelectron $\hat{\boldsymbol{k}}$. In what follows, we restrict our calculations to the polarization direction $\hat{\boldsymbol{k}} \| \hat{z}$ as is usually the case experimentally

We consider the inter-shell correlation which connects the transition in the outer shell $i \to k$ with the inner shell transition $j \to p$. The correlation-affected outer shell amplitude is expressed by the same Eq. (3) in which the reduced dipole matrix element d_{ik} is substituted with the solution of the integral equation:

$$D_{ik}(\omega) = d_{ik} + \frac{1}{3} \sum\!\!\!\!\!\!\!\int_p \frac{D_{jp} V_{ik,jp}}{\omega + \epsilon_j - \epsilon_p + i\delta} \ , \quad (5)$$

where a positive infinitesimal $+i\delta$ denotes the bypass of the real pole of the denominator in the complex energy half-plane. Furthermore, d_{ik} is a dipole matrix element in the absence of correlation given by Eq. (4) and $V_{ik,jp} = 2U_{ik,jp} - U_{ij,kp}$ is the Coulomb matrix containing the direct and exchange parts. The direct Coulomb matrix is expressed as

$$\begin{aligned} U_{ik,jp} \ &= \ \hat{\ell}\hat{\ell}' \, \hat{\ell}_i \, \hat{\ell}_j \begin{pmatrix} \ell & 1 & \ell_i \\ 0 & 0 & 0 \end{pmatrix} \begin{pmatrix} \ell' & 1 & \ell_j \\ 0 & 0 & 0 \end{pmatrix} \\ &\times \ R^{(1)}_{\ell,\ell',\ell_i,\ell_j}(k, p, n_i, n_j) \ , \end{aligned} \quad (6)$$

where $R^{(1)}$ is a Slater integral [1]. In the exchange matrix, the electron $k\ell$ and the hole $n_j\ell_j$ states are swapped. By definition, both the dipole and Coulomb matrices are real quantities. The fraction 1/3 in Eq. (5) is the result of the angular momentum projection summation. The symbol $\sum\!\!\!\!\!\!\int$ denotes the integration over the continuum spectrum $\int d\epsilon_p$ and the sum over the discrete spectrum $\sum_p$ of the inner shell excitations. Since i and j refer to to the outer and inner shell, respectively, the corresponding ionization potentials satisfy the relation $I_i = |\epsilon_i| \ll I_j = |\epsilon_j|$. In the case of a deep inner shell, its energy should be augmented by an Auger decay width and an infinitesimal δ should be replaced with a finite half width $\gamma_j/2$.

The partial photoionization cross section in RPAE is prportional to the absolute square of the dipole matrix element (5)

$$\sigma_{ik}(\omega) = \frac{4}{3} \pi^2 \alpha a_0^2 \omega |D_{ik}|^2 \quad (7)$$

Here α is the fine structure constant and a_0 is the Bohr radius. The analogous expression with a non-correlated matrix element d_{ik} gives the value which we refer to as the Hartree-Fock approximation.

B. Lowest order perturbation theory

Even though Eq. (5) can be solved numerically to a sufficient accuracy, we provide a simplified treatment which is less accurate but much more physically transparent. In the case of a weak inter-shell correlation, which is typically the case between the inner and outer shells, the correlated matrix element of the inner shell photoionization in the rhs of Eq. (5) can be approximated by its uncorrelated value, and the exchange part of the Coulomb interaction can be dropped, hence

$$D_{ik}(\omega) = d_{ik} + \frac{2}{3} \sum\!\!\!\!\!\!\!\int_p \frac{d_{jp}U_{ik,jp}}{\omega+\epsilon_j-\epsilon_p+i\delta} \equiv d_{ik} + \Delta d_{ik} \quad (8)$$

We further rewrite the correlation induced part of the dipole matrix of the outer shell as

$$\Delta d_{ik} = 4\sum_{p=1}^{\infty} \frac{a_p}{\omega+\epsilon_j-\epsilon_p} + \int_0^\infty d\epsilon \frac{a(\epsilon)}{\omega+\epsilon_j-\epsilon+i\delta} \ , \quad (9)$$

where we introduce $a_p \equiv (2/3) d_{jp}U_{ik,jp}$ and its continuous spectrum counterpart $a(\epsilon)$ for brevity of notation. We split the principal value and the singular part of the integral

$$\int_0^\infty \frac{a(\epsilon)\ d\epsilon}{\omega+\epsilon_j-\epsilon+i\delta} = P\int_0^\infty \frac{a(\epsilon)\ d\epsilon}{\omega+\epsilon_j-\epsilon} - i\pi a(\omega_{ik}+\epsilon_j) \quad (10)$$

where $\omega_{ik} = \epsilon_k - \epsilon_i$ is the energy of the outer shell transition. Near the inner shell threshold, $\omega + \epsilon_j = 0$, the principal value integral is logarithmically divergent at the lower limit. However, this divergence is compensated for by the infinite part of the discrete sum. Indeed, because of the continuity of the oscillator strength across the ionization threshold,

$$\lim \frac{a_p}{\epsilon_{p+1}-\epsilon_p}\Big|_{p\to\infty} = a(\epsilon=0)$$

and then absorb an infinite part of the sum into the integral:

$$\begin{aligned} \Delta d_{ik} &= \sum_{p=1}^{N\gg 1} \frac{a_p}{\omega+\epsilon_j-\epsilon_p} + \int_{\Delta<0}^{\infty} d\epsilon \frac{a(\epsilon)}{\omega+\epsilon_j-\epsilon+i\delta} \\ &\qquad - i\pi a(\omega_{ik}+\epsilon_j) \ , \qquad (11) \end{aligned}$$

where we introduced a shift of the threshold by a small quantity Δ. The remaining finite sum in the right-hand side of Eq. (11) describes the series of the auto-ionizing states below the threshold. We omit this region from our consideration and concentrate on the above-threshold ionization. After the divergence in the principal value of the integral term is isolated and removed, the small regular part can be ignored in comparison with the direct photoionization matrix element because of the weakness of the correlation. With this in mind, we write the dipole matrix element of the outer shell photoionization near the inner shell threshold as

$$\begin{aligned} D_{ik} &= d_{ik} - i(2/3)\pi d_{jp}U_{ik,jp} \qquad (12) \\ \arg D_{ik} &= -\arctan \frac{2}{3}\ \frac{\pi d_{jp}U_{ik,jp}}{d_{ik}} \ , \end{aligned}$$

where the continuous states in both transitions are bound by the energy conservation $\epsilon_k - \epsilon_i = \epsilon_p - \epsilon_j$. Eq. (12) gives the lowest order perturbation theory (LOPT) estimate for the correlation induced phase of the ionization amplitude.

C. Relativistic extensiton

The relativistic photoionization theory should take into account the spin-orbit splitting of atomic shells. The relativistic counterpart of the RPAE, the relativistic random phase approximation (RRPA) considers a one-electron transition from an initial state characterized by the quantum numbers $n\,ljm$ to a final continuum state $\hat{\boldsymbol{k}}\,\bar{l}\,\bar{j}\,\bar{m}$. The relativistic counterpart of Eq. (3) is the electric dipole amplitude which, for a linearly polarized light, is given by Eqs. (7-8) of [16]:

$$\begin{aligned} T^{1\nu}_{nljm} &= \sum_{\bar\kappa\bar m} C^{j\bar m}_{l,\bar m-\nu,\frac12\nu} Y_{l\bar m-\nu}(\hat{\boldsymbol{k}}) \\ &\times (-1)^{2\bar j+j+1-\bar m} \begin{pmatrix} \bar j & 1 & j \\ -\bar m & 0 & m \end{pmatrix} i^{1-\bar l} e^{i\delta_{\bar\kappa}} \left\langle \bar a \| Q_1^{(1)} \| a \right\rangle \\ &\qquad (13) \end{aligned}$$

Here and below we use the notation $\kappa = \mp(j+\frac12)$ for $j = l\pm\frac12$, $\nu = \pm 1/2$ is the photoelectron spin polarization, the C's are the Clebsch-Gordon coefficients and the Y's are the spherical harmonics. We will also use an asterisk for the lower j component of a spin-orbit doublet, $j = l - \frac12$, e.g., $np_{1/2} \equiv np^*$. The reduced matrix element of the spherical tensor between the initial state $a = (n\kappa)$ and a final state $\bar a = (\epsilon, \bar\kappa)$ is obtained from a solution of the set of the integral RRPA equations similar to the RPAE Eq. (5). For the brevity of notation, we absorb the phase factor into the reduced matrix element

$$D_{lj\to\bar l\bar j} = i^{1-\bar l} e^{i\delta_{\bar\kappa}} \left\langle \bar a \| Q_J^{(\lambda)} \| a \right\rangle \quad (14)$$

In the polarization axis direction $\hat{\boldsymbol{k}} \| \hat z$, only the axial, Y_{l0},components of the spherical harmonics in Eq. (13) are non-zero, so only terms with $m = \nu = \pm 1/2$ survive. Due to the axial symmetry, then, the final result does not depend on the sign of the spin and the angular momentum projections. The expressions below show the axial components of the relativistic ionization amplitudes for the ns, np and nd initial states,

$$\begin{aligned}
T^{(1)}_{ns_{1/2}} &= -\frac{1}{3\sqrt{2}} Y_{10} D_{ns_{1/2}\to\epsilon p_{1/2}} - \frac{1}{3} Y_{10} D_{ns_{1/2}\to\epsilon p_{3/2}} \\
T^{(1)}_{np_{1/2}} &= \frac{1}{\sqrt{15}} Y_{20} D_{np_{1/2}\to\epsilon d_{3/2}} + \frac{1}{\sqrt{6}} Y_{00} D_{np_{1/2}\to\epsilon s_{1/2}} \\
T^{(1)}_{np_{3/2}} &= \frac{1}{\sqrt{6}} Y_{00} D_{np_{3/2}\to\epsilon s_{1/2}} - \frac{1}{5\sqrt{6}} Y_{20} D_{np_{3/2}\to\epsilon d_{3/2}} \\
&\quad -\frac{1}{5}\sqrt{\frac{3}{2}} Y_{20} D_{np_{3/2}\to\epsilon d_{5/2}} \qquad (15) \\
T^{(1)}_{nd_{3/2}} &= -\frac{1}{3\sqrt{2}} Y_{10} D_{nd_{3/2}\to\epsilon p_{1/2}} + \frac{1}{3}\sqrt{\frac{1}{10}} Y_{10} D_{nd_{3/2}\to\epsilon p_{3/2}} \\
&\quad +\sqrt{\frac{3}{70}} Y_{30} D_{nd_{3/2}\to\epsilon f_{5/2}} \\
T^{(1)}_{nd_{5/2}} &= \frac{1}{\sqrt{15}} Y_{10} D_{nd_{5/2}\to\epsilon p_{3/2}} - \frac{1}{7\sqrt{10}} Y_{30} D_{nd_{5/2}\to\epsilon f_{5/2}} \\
&\quad -\frac{\sqrt{2}}{7} Y_{30} D_{nd_{5/2}\to\epsilon f_{7/2}}
\end{aligned}$$

with the spherical harmonics in Eq. (15) are taken in the $\hat{z}$ direction i.e., $\theta = 0$. The complete set of amplitudes for an arbitrary direction, including the off-axial terms is given in [16, 17].

D. Time delay

Each amplitude in Eq. (15) is associated with its own Wigner time delay defined as

$$\tau_{nlj} = \frac{d\eta_{nlj}}{d\epsilon} \ , \ \eta_{nlj} = \tan^{-1}\left[\frac{\mathrm{Im} T^{(1)}_{nlj}(\hat{\boldsymbol{k}}\|\hat{z})}{\mathrm{Re} T^{(1)}_{nlj}(\hat{\boldsymbol{k}}\|\hat{z})}\right] \ , \ \epsilon = k^2/2 \ . \tag{16}$$

In the case when spin-orbit components are not resolved as in light atoms, the average time delay should be evaluated as a weighted average [18]

$$\bar{\tau}_{nl} = \frac{\sum_j \tau_{nlj}\sigma_{nlj}}{\sum_j \sigma_{nlj}} \ . \tag{17}$$

In a weakly relativistic limit, it tends to its non-relativistic counterpart

$$\tau_{nl} = \frac{\partial \arg f_{nl}(\hat{\boldsymbol{k}}\|\hat{z})}{\partial \epsilon} \ , \tag{18}$$

where the amplitude $f_{nl}(\hat{\boldsymbol{k}})$ is given by Eq. (3). We also note that the photoelectron in each partial wave has its own group delay which can be calculated as

$$\tau_{nlj\to\epsilon\bar{l}\,\bar{j}} = \frac{\partial \arg D_{nlj\to\epsilon\bar{l}\,\bar{j}}}{\partial \epsilon} \ . \tag{19}$$

Because individual partial waves are not presently resolved experimentally, it is the time delay (16) that is of our prime interest. It is instructive, nevertheless, to analyze the group delays in various individual photoelectron channels and to see how they combine to form the group delay for a particular relativistic subshell nlj or, equivalently, nl and nl^*.

III. RESULTS AND DISCUSSION

In the following we consider several typical examples of outer shell photoionization near inner shell thresholds: Ne $2p$ photoionization near the $1s$ threshold, Ar $3s$ and $2p$ photoionization near the $2p^*$ threshold and Kr $3d$ photoionization near the $2p$ and $2p^*$ thresholds.

A. Neon $2p$ photoionization near the $1s$ threshold

To elucidate the role of the inter-shell correlation in the valence shell photoionization of neon, we carry out two sets of RRPA calculations. In one calculation, we use the complete set of 9 relativistic coupled channels:

$$\begin{aligned}
1s_{1/2} &\to \epsilon p_{1/2},\ \epsilon p_{3/2} \\
2s_{1/2} &\to \epsilon p_{1/2},\ \epsilon p_{3/2} \\
2p^* \equiv 2p_{1/2} &\to \epsilon s_{1/2},\ \epsilon d_{3/2} \\
2p \equiv 2p_{3/2} &\to \epsilon s_{1/2},\ \epsilon d_{3/2},\ \epsilon d_{5/2}
\end{aligned}$$

In a second truncated 7-channel calculation, the transitions from the K-shell $1s_{1/2} \to \epsilon p_{1/2},\ \epsilon p_{3/2}$ are omitted. In the complete RPAE calculation, we include all four non-relativistic channels: $1s \to \epsilon p$, $2s \to \epsilon p$ and $2p \to \epsilon s, d$. By making a comparison between the results of the complete and truncated calculations, we clearly identify the effect of the inner channel openings on the cross section and time delay of the outer shells.

Results of these calculations are displayed in Fig. 1 where we show the partial $2p$ photoionization cross section as a function of the excess energy near the $1s$ threshold. We observe that the truncated RRPA calculation is smooth across the threshold whereas the full calculation is broken by a series of auto-ionizing resonances below the threshold, while above the threshold, the cross section is a smooth function again, deviating insignificantly from the truncated result by about 10%.

Simultaneously, however, the inter-shell correlation affects the phase of the $2p$ photoionization amplitude in a very significant way. This phase above the $1s$ threshold is shown in the top panel of Fig. 2, as a function of the excess energy, with logarithmic energy scale for clarity. Here the complete 9-channel RRPA result varies quite considerably whereas the corresponding 7-channel RRPA phase is essentially flat. The 9-channel RRPA phase variation is also very close to the LOPT prediction. In other words, without coupling with the $1s$ channels, the phase of the $2p$ photoionization amplitude is nearly zero and hardly varies with energy; with the coupling, the phase is significant, and varies considerably with energy.

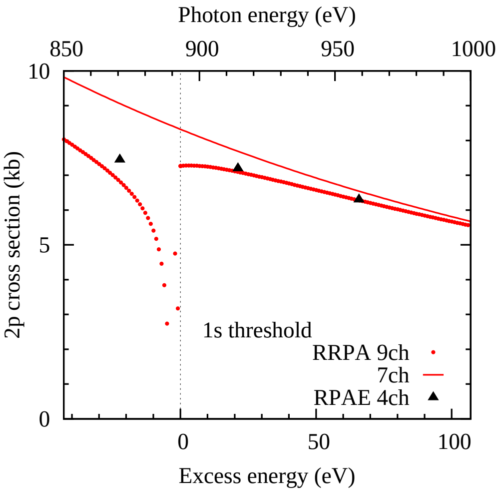

FIG. 1: Photoionization cross section of the $2p$ shell of Ne near the $1s$ threshold as a function of the excess energy, the energy with respect to the $1s$ threshold. The complete 9-channel and the truncated 7-channel RRPA calculations are shown with the (red) dots and solid line, respectively. The 4-channel RPAE calculation from [15] is shown with filled triangles.

In the middle panel of Fig. 2, the phase is converted to the Wigner time delay using Eq. (16). The $2p_{1/2}$ and $2p_{3/2}$ components of the time delay are indistinguishable on the scale of the figure. For a better differentiation accuracy in the vicinity of the threshold, the 9-channel RRPA phase is fitted with the exponential-polynomial ansatz

$$\phi(E[\mathrm{eV}]) = \exp[-bE](a_0 + a_1E + a_2E^2) \qquad (20)$$

and the time delay at the threshold is expressed as

$$\tau(E=0)[\mathrm{as}] = (-ba_0 + a_1) \times 2\mathrm{Ry} \times 24.2(\mathrm{as}) \qquad (21)$$

For the $2p$ shell of Ne this expression returns $\tau_{2p_{1/2}}(E = 0) = 8.37$ as and $\tau_{2p_{3/2}}(E = 0) = 8.34$ as. Note that, owing to the approximate nature of the extrapolation process, sub-attosecond differences are not considered to be physically meaningful. The time delay in the truncated 7-channel RRPA calculation is virtually zero on the scale of the figure. Hence, all the observed time delay in the complete RRPA calculation is due to the $1s/2p$ inter-channel correlation. In the bottom panel of Fig. 1, the time delay is shown on the linear photon energy scale. We see that the rise of the time delay near the threshold is rather steep and the precise value at the threshold is difficult to determine.

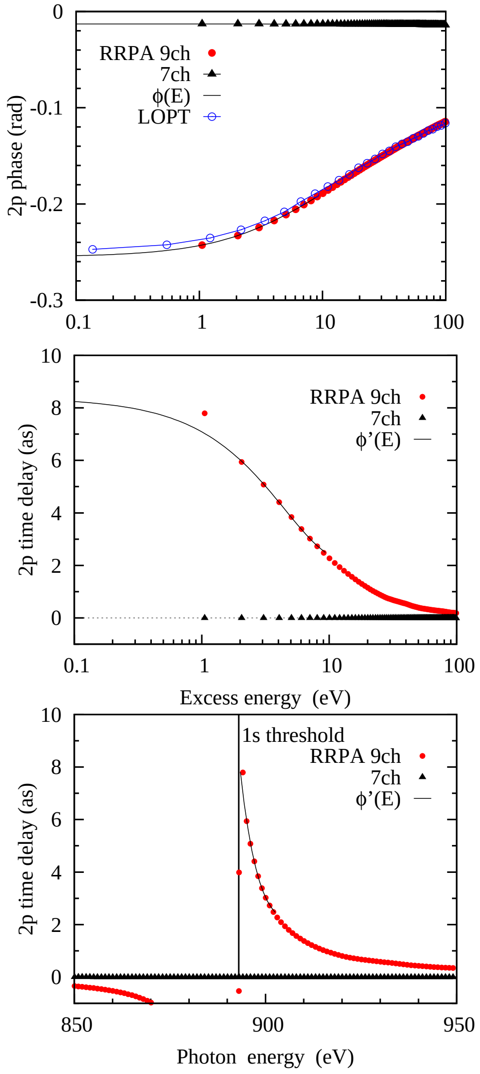

FIG. 2: Top: Phase of the $2p$ photoionization amplitude of Ne near the $1s$ threshold from the complete 9-channel RRPA calculation is shown with (red) filled circles while its analytic fit with Eq. (20), $\phi(E)$, is shown with (red) solid line. The same phase from a truncated 7-channel RRPA calculation is shown with triangles. The LOPT calculation is displayed with open (blue) circles joined by the solid line to guide the eye. Middle: Phase of the photoionization amplitude, converted to the Wigner time delay using Eq. (16) and displayed with the same symbols. Bottom: Same as Middle but on a linear photon energy scale.

The threshold group delays in various photoelectron partial waves are tabulated in Table I. The log scale results refer to Eq. (21) while the linear scale results are obtained by estimating threshold intercept. Both sets of results are quite close. We note that the s-wave has negative group delay whereas the d-waves have positive time delay. This sign inversion follows from the $(-1)^{\ell_{\max}}$ rule since $\ell_{\max} = 1$ for $p \to s$ transition and $\ell_{\max} = 2$ for $p \to d$. As the d-waves are strongly dominant due to the Fano propensity rule [19], the net Wigner time delay for the $2p_{1/2}$ and $2p_{3/2}$ subshells is close to that of the photoelectron group delay in the d partial waves because the corresponding terms are dominant in the subshell photoionization amplitudes (15).

The negative phase, decreasing in magnitude with excess energy, which is converted to a positive time delay as shown in Fig. 2 can be understood from the LOPT

TABLE I: Photoelectron group delays (19) and Wigner time delays (16) of the $2p_{1/2}$ and $2p_{3/2}$ shells of Ne at the $1s$ threshold, in attoseconds, from the full 9-channel RRPA calculation. The Dirac-Fock $E_{\rm DF}$ and experimental $E_{\rm exp}$ [20] threshold energies are displayed.

Channel	Delay (as)	
Energy scale	Log	Linear
Ne $1s$ threshold		
$E_{\rm DF} = 893$ eV		
$E_{\rm exp} = 870$ eV		
$2p^* \equiv 2p_{1/2} \to \epsilon d_{3/2}$	9.28	9.00
$2p_{1/2} \to \epsilon s_{1/2}$	-5.77	-5.87
$2p_{1/2}$ total	8.37	
$2p_{3/2} \to \epsilon d_{3/2}$	9.20	8.88
$2p_{3/2} \to \epsilon d_{5/2}$	9.31	9.06
$2p_{3/2} \to \epsilon s_{1/2}$	-5.85	-5.97
$2p_{3/2}$ total	8.34	

equation (12). We see that the sign of the correlation-induced phase depends on the sign of the three matrix elements: the two dipole matrices in the outer d_{ik} and inner d_{jp} channels and the Coulomb interaction $U_{ik,jp}$. In the present case we consider the strongest outer channel $2p \to \epsilon d$ and correlate it with the inner channel $1s \to \epsilon p$. The corresponding dipole matrix elements near the $1s$ threshold are exhibited in Fig. 3. From this figure we observe that $d_{2p\to\epsilon d} > 0$ while $d_{1s\to\epsilon p} < 0$. The sign of these matrix elements is determined by the angular factor in Eq. (4):

$$\hat{l}\hat{l}_i \begin{pmatrix} l & 1 & l_i \\ 0 & 0 & 0 \end{pmatrix} \equiv \hat{l}_{\rm max}(-1)^{l_{\rm max}} \quad , \quad l_{\rm max} = \max(l, l_i) \qquad (22)$$

Indeed, the radial integral in Eq. (4), which contains the nodeless orbitals $1s$ and $2p$, is always positive near the threshold. The angular part of the Coulomb matrix is given by the product of the angular parts of the dipole matrices of the interacting channels (see Eq. (8) in [14]). Hence the Coulomb interaction matrix $U_{1s\epsilon p,2p\epsilon d}$ is also negative near the threshold. Therefore both the numerator and the denominator in the LOPT expression for the phase (12) are positive and given the minus sign before the ratio the phase itself is negative. While the matrices $d_{2p\to\epsilon d}$ and $U_{1s\epsilon p,2p\epsilon d}$ are rather flat, the dipole matrix $d_{1s\to\epsilon p}$ is noticeably decreasing away from the threshold. Hence the LOPT phase is decreasing in magnitude also. The corresponding time delay is positive and diminishes rapidly as the excess energy grows.

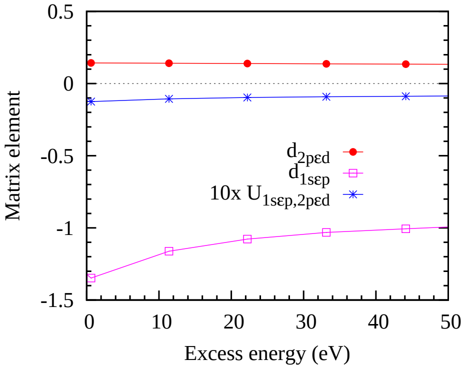

FIG. 3: Dipole matrix elements $d_{1s\epsilon p}$ and $d_{2p\epsilon d}$ for the inner and outer ionization channels in Ne, shown as (red) filled circles and (purple) open squares, respectively. The Coulomb interaction matrix $U_{1s\epsilon p,2p\epsilon d}$ (multiplied by 10) is shown as (blue) asterisks.

B. Argon near the $2p^*$ threshold

The complete RRPA calculation on argon contains 16 relativistic channels:

$$\begin{array}{rcl} 1s_{1/2} & \to & \epsilon p_{1/2},\ \epsilon p_{3/2} \\ 2s_{1/2} & \to & \epsilon p_{1/2},\ \epsilon p_{3/2} \\ 2p^* \equiv 2p_{1/2} & \to & \epsilon s_{1/2},\ \epsilon d_{3/2} \\ 2p\ \ \equiv 2p_{3/2} & \to & \epsilon s_{1/2},\ \epsilon d_{3/2},\ \epsilon d_{5/2} \\ 3s_{1/2} & \to & \epsilon p_{1/2},\ \epsilon p_{3/2} \\ 3p^* \equiv 3p_{1/2} & \to & \epsilon s_{1/2},\ \epsilon d_{3/2} \\ 3p\ \ \equiv 3p_{3/2} & \to & \epsilon s_{1/2},\ \epsilon d_{3/2},\ \epsilon d_{5/2} \end{array}$$

In a truncated 14-channel calculation, the $2p^*$ ionization channels are removed to demonstrate clearly the inner threshold effect. In the further trimmed 11-channel calculation, the $2p$ ionization channels are dropped. In the RPAE calculation, we include 6 non-relativistic channels: $2s \to \epsilon p$, $2p \to \epsilon s, d$, $3s \to \epsilon p$, $3p \to \epsilon s, d$.

1. *3s photoionization*

Results of these calculations for the $3s$ cross section near the $2p^*$ threshold are shown in Fig. 4. In the complete RRPA calculation, a smooth cross section is interruputed by a series of auto-ionizing resonances below the threshold (not fully resolved in the figure). In a truncated 14-channel calculation, the resonant region is located below the $2p$ threshold. In a further truncated 11-channel RRPA calcualtion, all the resonances are removed and the cross section is smooth across the threshold region.

In the top panel of Fig. 5 we show the phase of the $3s$ photoionization amplitude from the 16-, 14- and 11-channel RRPA calculations and the LOPT value from Eq. (12). The RRPA phases are fitted with the ansatz (20) and differentiated analytically to produce the time

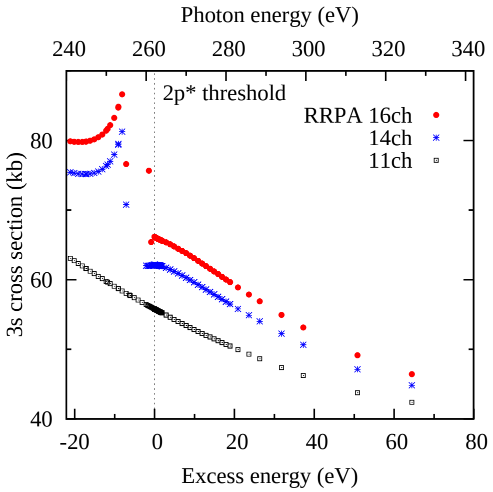

FIG. 4: Photoionization cross section of the $3s$ shell of Ar near the $2p^*$ threshold as a function of the excess energy. The complete 16-channel and the truncated 14- and 11-channel RRPA calculations are shown as (red) dots, (blue) asterisks and open squares, respectively.

delays shown in the middle panel of the figure. The $3s$ time delay near the $2p$ threshold is negative. The threshold values are -19.7 as, -9.4 as and -1.9 as in the complete and the two truncated RRPA calculations, respectively. Thus by removing the inter-shell correlation of the sub-valence $3s$ shell with the inner $2p$ and $2p^*$ shells, the time delay is significantly reduced. To highlight the utility of the analytical interpolation and differentiation, we show the raw numerical data of the $3s$ time delay in the bottom panel on the linear photon energy scale from which estimating the value at the threshold results in a greater numerical noise.

The energy variation of the LOPT phase, Eq. (12), near the threshold is very similar to the complete RRPA calculation. To elucidate the sign of the LOPT phase and its energy dependence, we examine the inner and outer transitions along with their Coulomb interaction. The corresponding dipole matrix elements are exhibited in Fig. 6. We see that the signs of the inner and outer dipole matrix elements are now inverted as compared with the case of Ne shown in Fig. 3. The outer dipole matrix element $d_{3s\to\epsilon p} < 0$ while the inner matrix element $d_{2p\to\epsilon d} > 0$, as prescribed by the signs of their respective angular factors, Eq. (22). As the Coulomb matrix element is positive in this case, the LOPT phase is positive also and is rapidly decreasing away from the threshold. This behavior produces a large negative time delay at the inner-shell threshold.

2. $3p$ photoionization

The photoionization cross section of the valence $3p$ shell near the $2p^*$ threshold is shown in Fig. 7. Unlike the threshold behavior of the $2p$ cross section near the $1s$ threshold in Ne (Fig. 1) and the $3s$ cross section near the $2p^*$ threshold in Ar (Fig. 4), the variation of the $3p$ cross section above the $2p^*$ threshold is rather small when the number of coupled channels the RRPA calculation changes. This insensitivity of the cross section to the inter-shell correlation is reflected in the threshold behavior of the time delay which is exhibited in Fig. 8.

The phases in the individual photoelectron partial waves and the net phase of the photoionization ampli-

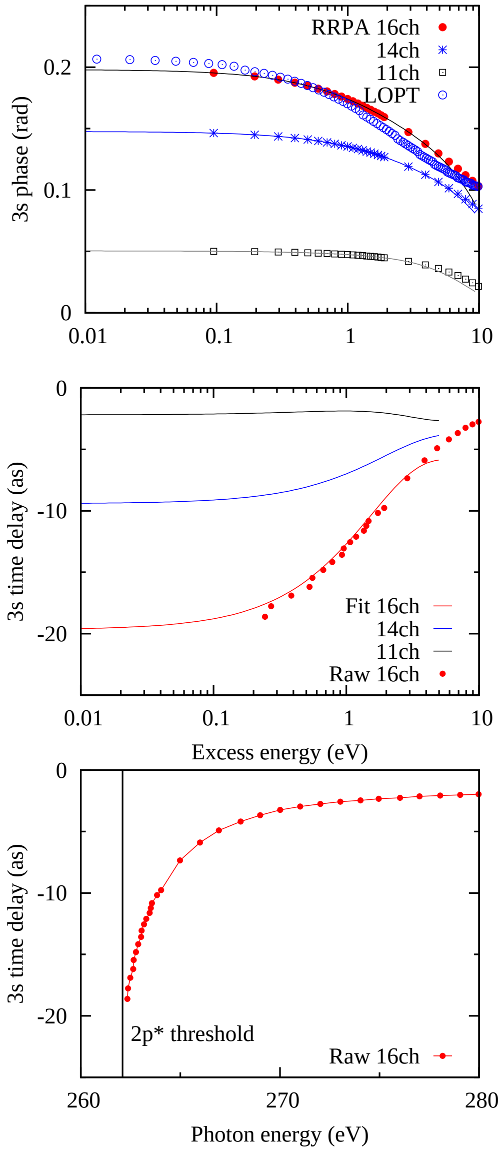

FIG. 5: Top: Phase of the $3s$ photoionization amplitude of Ar near the $2p^*$ threshold from the 16-, 14- and 11-channel RRPA calculations, shown as (red) filled circles, (blue) asterisks and open squares. The analytic fit using Eq. (20) is shown with similarly colored solid lines. The LOPT calculation is displayed as (blue) open circles. Middle: Analytic fit to the phase of the photoionization amplitude, converted to Wigner time delay using Eq. (1). Bottom: Time delay from the 16-channel RRPA calculation shown on a linear photon energy scale.

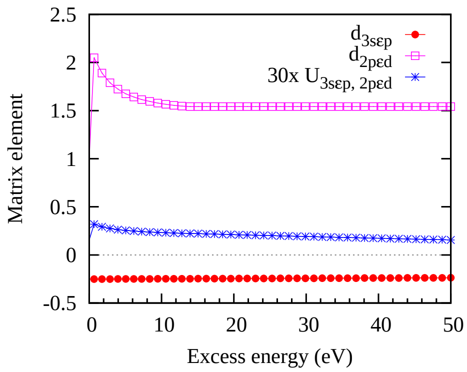

FIG. 6: Dipole matrix elements $d_{3s\epsilon p}$ and $d_{2p\epsilon d}$ for the inner and outer ionization channels of Ar, shown as (red) filled circles and (purple) open squares, respectively. The Coulomb interaction matrix $U_{3s\epsilon p,2p\epsilon d}$ (multiplied by 30) is shown as (blue) asterisks.

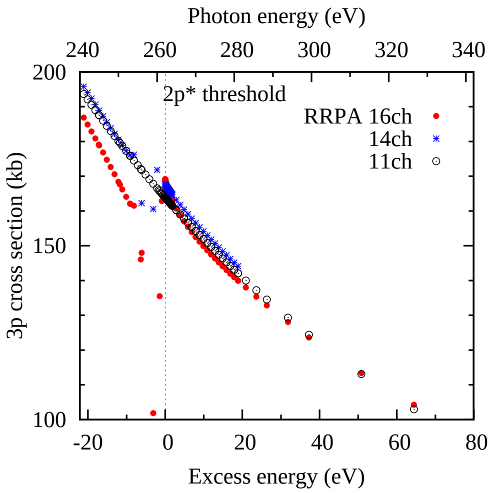

FIG. 7: Photoionization cross section of the $3p$ shell of Ar near the $2p^*$ threshold as a function of excess energy. The complete 16-channel and the truncated 14- and 11-channel RRPA calculations are shown as (red) dots, (blue) asterisks and open circles, respectively.

tude for the $3p_{1/2}$ subshell of Ar are depicted in the top panel of Fig. 8 as functions of the photoelectron energy. These phases, when converted to the photoelectron group delays (19) and the net Wigner time delay (16) are displayed in the bottom panel of this figure. As in the case of the Ne $2p$ shell, the group delay is negative for the s-continuum and positive for the d-continuum.

Unlike in the Ne $2p$ shell, where the d-waves dominate the Wigner time delay, various continua compensate for each other in the case of Ar $3p_{1/2}$. While the threshold group delay is large and negative for the ϵs continuum, it is small and positive for the ϵd continuum and small and negative for the net Wigner time delay. The corresponding values of the group and Wigner time delays at the threshold are given in Table II. Reading these values

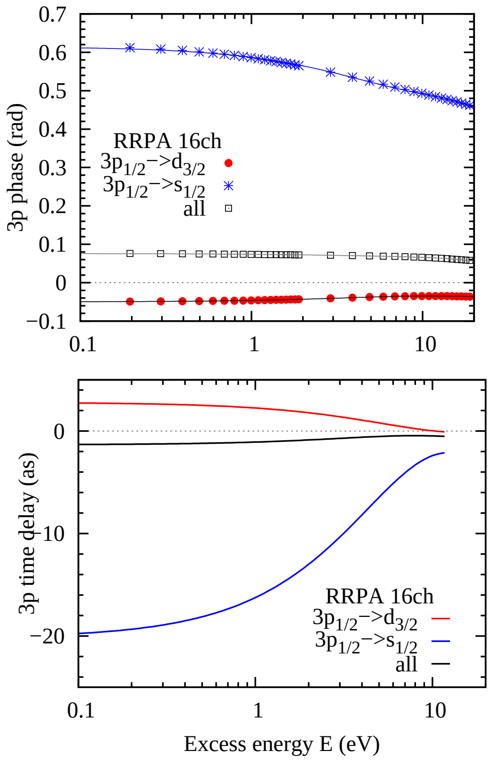

FIG. 8: Top: Phase of the various $3p_{1/2}$ photoionization amplitudes of Ar near the $2p^*$ threshold: $3p_{1/2} \to \epsilon d_{3/2}$ - (red) filled circles, $3p_{1/2} \to \epsilon s_{1/2}$ - (blue) asterisks, sum over all final channels - open squares. The analytic fit using Eq. (20) is shown with similarly colored solid lines. Bottom: Analytic fit to the phase of the photoionization amplitudes, converted to the group delay (19) and Wigner time delay (1)

we observe that a small effect of inter-shell correlation on the photoionization cross section is commensurate with a similarly insignificant effect of the correlation on the Wigner time delay.

TABLE II: Photoelectron group delays (19) and Wigner time delays (16) of the $3s$ and $3p$ shells of Ar at the $2p^*$ threshold from the full 16-channel RRPA calculation. The Dirac-Fock $E_{\rm DF}$ and experimental $E_{\rm exp}$ [20] threshold energies are displayed.

Channel Energy scale	Delay (as) Log	 Linear
Ar $2p^*$ threshold		
$E_{\rm DF} = 262$ eV		
$E_{\rm exp} = 250$ eV		
$3p_{1/2} \to \epsilon d_{3/2}$	2.8	2.8
$3p_{1/2} \to \epsilon s_{1/2}$	-20.2	-24.1
$3p_{1/2}$ total	-3.5	
$3p_{3/2} \to \epsilon d_{3/2}$	10.0	12.7
$3p_{3/2} \to \epsilon d_{5/2}$	10.0	12.7
$3p_{3/2} \to \epsilon s_{1/2}$	-17.8	-21
$3p_{3/2}$ total	1.7	
$3s_{1/2} \to \epsilon p_{1/2}$	-18.3	-16.6
$3s_{1/2} \to \epsilon p_{3/2}$	-20.3	-14.9
$3s_{1/2}$ total	-19.7	

TABLE III: Photoelectron group delays and Wigner time delays of the $3d$ and $3d^*$ shells of Kr at the $2p$ and $2p^*$ thresholds. The Dirac-Fock $E_{\rm DF}$ and experimental $E_{\rm exp}$ [20] threshold energies are shown.

Channel Energy scale	Delay (as) Log	 Lin	Channel Energy scale	Delay (as) Log	 Lin
2p* threshold			2p threshold		
$E_{\rm DF} = 1,765$ eV			$E_{\rm DF} = 1,711$ eV		
$E_{\rm exp} = 1,730$ eV			$E_{\rm exp} = 1,678$ eV		
$3d_{3/2} \to \epsilon p_{1/2}$	-14.80	-13.95	$3d_{3/2} \to \epsilon p_{1/2}$	-31.63	-28.19
$3d_{3/2} \to \epsilon p_{3/2}$	-36.15	-34.28	$3d_{3/2} \to \epsilon p_{3/2}$	-13.80	-11.80
$3d_{3/2} \to \epsilon f_{5/2}$	3.93	3.75	$3d_{3/2} \to \epsilon f_{5/2}$	27.56	25.87
$3d_{3/2}$ total	0.29		$3d_{3/2}$ total	17.86	
$3d_{5/2} \to \epsilon p_{3/2}$	-14.5	-13.58	$3d_{5/2} \to \epsilon p_{3/2}$	-33.14	-29.64
$3d_{5/2} \to \epsilon f_{5/2}$	9.10	8.92	$3d_{5/2} \to \epsilon f_{5/2}$	19.49	17.69
$3d_{5/2} \to \epsilon f_{7/2}$	16.18	16.45	$3d_{5/2} \to \epsilon f_{7/2}$	17.77	16.72
$3d_{5/2}$ total	10.84		$3d_{5/2}$ total	9.35	

TABLE IV: Wigner time delays of various shells of Kr at several inner-shell thresholds

	Time delay (as)		
Threshold	$1s_{1/2}$	$2p_{1/2}$	$2p_{3/2}$
$E_{\rm DF}$, eV	14,413	1,765	1,711
$E_{\rm exp}$, eV	14,326	1,730	1,678
Shell			
$4p_{3/2}$	2.02	3.28	1.65
$4p_{1/2}$	2.26	-1.58	5.36
$3d_{5/2}$	6.87	10.84	9.35
$3d_{3/2}$	7.04	0.29	17.86
$3p_{3/2}$	2.90	3.18	0.99
$3p_{1/2}$	3.07	-2.40	5.35
$2p_{3/2}$	3.07	8.35	
$2p_{1/2}$	2.95		

C. Krypton

1. *3d shell near the 2p and 2p* thresholds*

Photoionization of the $3d$ shell of Kr near the $2p$ and $2p^*$ thresholds is remarkable as it displays the largest photoelectron group delays and the net Wigner time delays among all the noble gas atoms from Ne to Xe in the present study. Examples of the photoionization phase and its energy derivatives for the $3d_{3/2}$ and $3d_{5/2}$ subshells of Kr near the $2p^*$ threshold are shown in Fig. 9.

The corresponding threshold time delays and their counterparts near the $2p$ threshold are collected in Table III. We see that some group delays are as large as 30 as and the Wigner time delay of the $3d^*$ shell near the $2p$ threshold is close to 20 as. This result is quite remarkable as a large atomic time delay is predicted at photon energies in the hard x-ray regime. This delay results entirely from inter-shell correlation and is not caused by the Coulomb drag that affects slow photoelectrons near their ionization threshold [15].

The compilation of the threshold time delays in Kr is shown in Table IV where it is seen that shells other than $3d$ display modest time delays, not exceeding 10 as. The respective threshold time delays in Xe (not shown) are significantly smaller. Even the $3d$ delays in Xe are only of the order of few attoseconds.

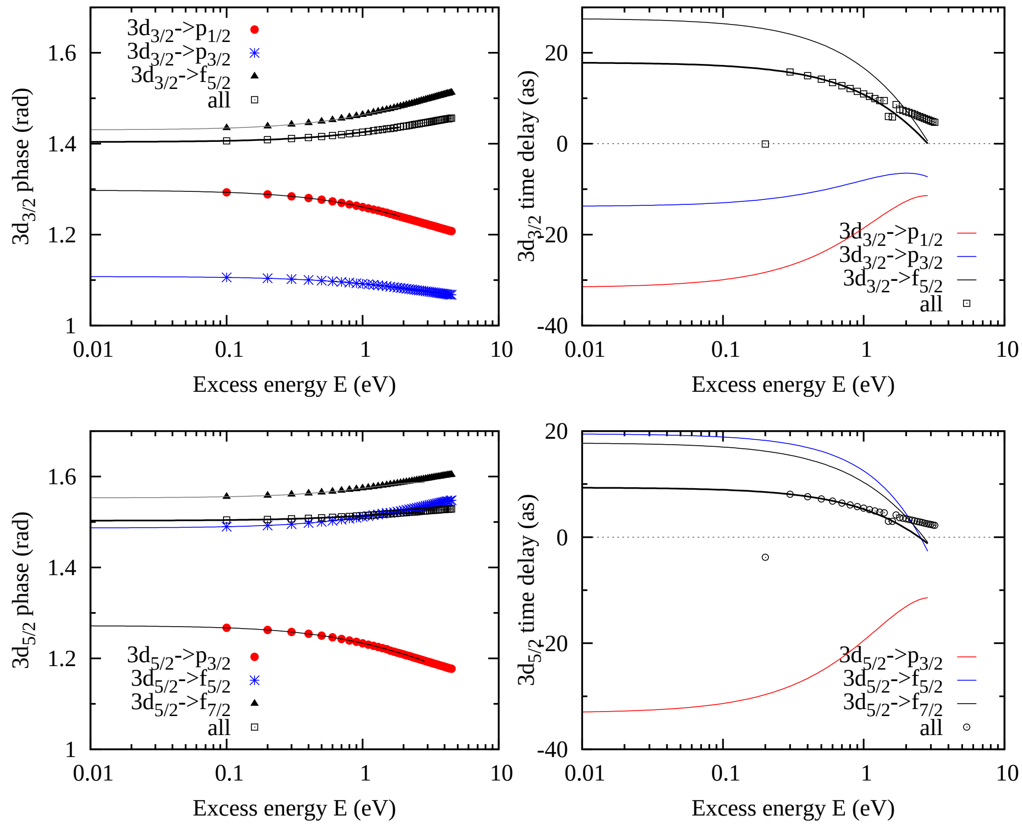

FIG. 9: Upper left: Phase of the various $3d_{3/2}$ photoionization amplitudes of Kr near the $2p_{1/2}$ threshold: $3d_{3/2} \to \epsilon p_{1/2}$ - (red) filled circles, $3d_{3/2} \to \epsilon p_{3/2}$ - (blue) asterisks, $3d_{3/2} \to \epsilon f_{5/2}$ - triangles and the $3d_{3/2}$ amplitude summed over all final channels - open squares. Upper right: Analytic fit using Eq. (20) shown with similarly colored solid lines and open squares for the $3d_{3/2}$ Wigner time delay. Bottom left: The same as above, but for $3d_{5/2} \to \epsilon p_{3/2}$ - (red) filled circles, $3d_{3/2} \to \epsilon f_{5/2}$ - (blue) asterisks, $3d_{5/2} \to \epsilon f_{7/2}$ - triangles and the summed $3d_{5/2}$ amplitude - open squares. Bottom right: Analytic fit using Eq. (20) shown with the similarly colored solid lines and open squares for the $3d_{5/2}$ Wigner time delay.

IV. SUMMARY AND CONCLUSIONS

In this work, we have demonstrated that Wigner time delay of outer atomic shells is affected, sometimes quite strongly, by correlation in the form of interchannel coupling with inner-shell photoionization channels in the vicinity of inner-shell thresholds. The phenomenology of this effect is quite rich. The jumps of the time delay near threshold can be quite small or quite large (as large as 36 as). In addition, the jumps due to interchannel coupling can be positive or negative. In other words, time delays that are so far above thresholds that they would have ordinarily gone to essentially zero, can be reactivated to significant values near the inner-shell thresholds owing to many-body interactions. Threshold time delay chronoscopy [21], thus, can be a significant tool in studying these correlation phenomena.

The results presented here provide a road map for experimental investigation of this phenomenology which can be implemented using recently developed technology. Attosecond streaking measurements can be expanded at present to the soft-x-ray water window [8]. We hope that with a rapid development of this technique, the most significant effects predicted here will be within the experimental reach in the near future. In addition, we have a good mathematical model for the signs and magnitudes of the various induced time delays, but not a good quantitative physical understanding of the phenomenon; but we hope these results will stimulate others to provide a physical model.

Acknowledgments

S.T.M. acknowledges the support of the Chemical Sciences, Geosciences and Biosciences Division, Office of Basic Energy Sciences, Office of Science, US Department of Energy under Grant No. DE-FG02-03ER15428.

---

[1] M. Y. Amusia, *Atomic photoeffect* (Plenum Press, New York, 1990).

[2] W. R. Johnson and C. D. Lin, *Multichannel relativistic random-phase approximation for the photoionization of atoms*, Phys. Rev. A **20**, 964 (1979).

[3] W. R. Johnson, C. D. Lin, K. T. Cheng, and C. M. Lee, *Relativistic random-phase approximation*, Physica Scripta **21**(3-4), 409 (1980).

[4] E. W. B. Dias, H. S. Chakraborty, P. C. Deshmukh, S. T. Manson, O. Hemmers, P. Glans, D. L. Hansen, H. Wang, S. B. Whitfield, D. W. Lindle, et al., *Breakdown of the independent particle approximation in high-energy photoionization*, Phys. Rev. Lett. **78**, 4553 (1997).

[5] M. Amusia, L. V. Chernysheva, and E. G. Drukarev, *Influence of the inner shell electrons on photoionization of outer shells*, The European Physical Journal D **69**(11), 245 (2015).

[6] E. P. Wigner, *Lower limit for the energy derivative of the scattering phase shift*, Phys. Rev. **98**(1), 145 (1955).

[7] M. Ossiander, F. Siegrist, V. Shirvanyan, R. Pazourek, A. Sommer, T. Latka, A. Guggenmos, S. Nagele, J. Feist, J. Burgdorfer, et al., *Attosecond correlation dynamics*, Nat. Phys. **13**, 280 (2017).

[8] S. L. Cousin, N. Di Palo, B. Buades, S. M. Teichmann, M. Reduzzi, M. Devetta, A. Kheifets, G. Sansone, and J. Biegert, *Attosecond streaking in the water window: A new regime of attosecond pulse characterization*, Phys. Rev. X **7**, 041030 (2017).

[9] M. Y. Amusia and L. V. Chernysheva, *Computation of atomic processes : A handbook for the ATOM programs* (Institute of Physics Pub., Bristol, UK, 1997).

[10] J. Dahlström, D. Guénot, K. Klünder, M. Gisselbrecht, J. Mauritsson, A. L. Huillier, A. Maquet, and R. Taïeb, *Theory of attosecond delays in laser-assisted photoionization*, Chem. Phys. **414**, 53 (2013).

[11] R. Pazourek, S. Nagele, and J. Burgdorfer, *Time-resolved photoemission on the attosecond scale: opportunities and challenges*, Faraday Discuss. **163**, 353 (2013).

[12] M. Y. Amusia, V. K. Ivanov, N. A. Cherepkov, and L. V. Chernysheva, *Interference effects in photoionization of noble gas atoms outer s-subshells*, Physics Letters A **40**(5), 361 (1972).

[13] M. Y. Amusia, V. Yarzhemsky, and L. Chernyshev, *Data for Photon Absorption, Electron Scattering, Vacancies Decay* (Springer, Berlin, 2012).

[14] A. S. Kheifets, *Time delay in valence-shell photoionization of noble-gas atoms*, Phys. Rev. A **87**, 063404 (2013).

[15] A. S. Kheifets, S. Saha, P. C. Deshmukh, D. A. Keating, and S. T. Manson, *Dipole phase and photoelectron group delay in inner-shell photoionization*, Phys. Rev. A **92**, 063422 (2015).

[16] A. Kheifets, A. Mandal, P. C. Deshmukh, V. K. Dolmatov, D. A. Keating, and S. T. Manson, *Relativistic calculations of angle-dependent photoemission time delay*, Phys. Rev. A **94**, 013423 (2016).

[17] A. Mandal, P. C. Deshmukh, A. S. Kheifets, V. K. Dolmatov, and S. T. Manson, *Angle-resolved Wigner time delay in atomic photoionization: The* 4*d subshell of free and confined Xe*, Phys. Rev. A **96**, 053407 (2017).

[18] Felix T. Smith, *Lifetime Matrix in Collision Theory*, Phys. Rev. **118**, 349 (1960).

[19] U. Fano, *Propensity rules: An analytical approach*, Phys. Rev. A **32**, 617 (1985).

[20] A. C. Thompson, D. T. Attwood, E. M. Gullikson, M. R. Howells, J. B. Kortright, A. L. Robinson, and J. H. Underwood, *X-ray data booklet* (Center for X-ray Optics and Advanced Light Source, Lawrence Berkeley National Laboratory, 2009).

[21] A. S. Kheifets, A. W. Bray, and I. Bray, *Attosecond time delay in photoemission and electron scattering near threshold*, Phys. Rev. Lett. **117**, 143202 (2016).